RSC Advances

PAPER

View Article Online
View Journal | View Issue

Cite this: *RSC Adv.*, 2018, **8**, 27144

Novel Mn^{4+}-activated $LiLaMgWO_6$ far-red emitting phosphors: high photoluminescence efficiency, good thermal stability, and potential applications in plant cultivation LEDs

Jia Liang, Liangling Sun, Balaji Devakumar, Shaoying Wang, Qi Sun, Heng Guo, Bin Li and Xiaoyong Huang *

Double perovskite-based $LiLaMgWO_6$:Mn^{4+} (LLMW:Mn^{4+}) red phosphors were synthesized by traditional solid-state route under high temperature, and they showed bright far-red emission under excitation of 344 nm. The crystal structure, luminescence performance, internal quantum efficiency, fluorescence decay lifetimes, and thermal stability were investigated in detail. All samples exhibited far-red emissions around 713 nm due to the $^2E_g \rightarrow {}^4A_{2g}$ transition of Mn^{4+} under excitation of near-ultraviolet and blue light, and the optimal doping concentration of Mn^{4+} was about 0.7 mol%. The CIE chromaticity coordinates of the LLMW:0.7% Mn^{4+} sample were (0.7253, 0.2746), and they were located at the border of the chromaticity diagram, indicating that the phosphors had high color purity. Furthermore, the internal quantum efficiency of LLMW:0.7% Mn^{4+} phosphors reached up to 69.1%, which was relatively higher than those of the reported Mn^{4+}-doped red phosphors. Moreover, the sample displayed good thermal stability; the emission intensity of LLMW:0.7% Mn^{4+} phosphors at 423 K was 49% of the initial value at 303 K, while the activation energy was 0.39 eV. Importantly, there was a broad spectral overlap between the emission band of LLMW:Mn^{4+} phosphors and the absorption band of phytochrome P_{FR} under near-ultraviolet light. All of these properties and phenomena illustrate that the LLMW:Mn^{4+} phosphors are potential far-red phosphors for applications in plant cultivation LEDs.

Received 3rd July 2018
Accepted 16th July 2018

DOI: 10.1039/c8ra05669b

rsc.li/rsc-advances

1. Introduction

Light-emitting diodes (LEDs) are used in many areas because of their high efficiency, energy saving properties, long lifetimes, and environmental friendliness.[1–15] Recently, the application of LEDs in plant cultivation has attracted worldwide attention. It is known that light is essential for plant growth, especially blue light (440 nm) and red light (660 nm), which can promote the synthesis of carbohydrates; in other words, both lights can act as the energy source to accelerate photosynthesis.[16–18] However, only these two lights are not sufficient. Researchers have shown that two types of phytochromes in plants have significant effects on the growth of plants; one is P_{FR}, which can switch to another type, P_R, by absorbing a certain amount of far-red light (730 nm), and P_R can also transform back to P_{FR} after exposure to red light (660 nm).[19,20] Please note that P_R is beneficial to the growth of short-day plants from seed germination to flowering and fruitage.[21] On the other hand, the ratio of P_{FR} and P_R can control the flowering time of plants. For ornamental plants, the precise blooming time is significant, which can be modulated by adjusting the ratio of P_{FR} and P_R through irradiation of red light and far-red light. Hence, far-red light plays an important role in plant cultivation. Although blue LEDs and red LEDs have already been studied extensively for plant cultivation, light at 730 nm is insufficient for plant growth. Thus, it is very challenging to find an efficient far-red light source for use in plant cultivation.

Currently, the non-rare-earth Mn^{4+} ion has been widely researched for white LEDs in general lighting applications due to its deep-red emitting wavelength.[22–32] Recently, it was reported that Mn^{4+} ions with a far-red emission of around 710 nm can also be used for plant cultivation LEDs because the emission range due to the $^2E_g \rightarrow {}^4A_{2g}$ transition was in accordance with the absorption band of phytochrome P_{FR} (centers at 730 nm).[33] Moreover, the Mn^{4+} ion can be excited by both blue and near-ultraviolet (NUV) LED chips and exhibits wide absorption bands, which broaden the application field. Compared with rare-earth ions, Mn^{4+} ions have some merits such as mild synthetic conditions, low price, and a deep red emission range. Due to all of these advantages, Mn^{4+} ions are extensively researched.

Key Lab of Advanced Transducers and Intelligent Control System, Ministry of Education and Shanxi Province, College of Physics and Optoelectronics, Taiyuan University of Technology, Taiyuan 030024, P. R. China. E-mail: huangxy04@126.com

In this study, we reported the synthesis and luminescence properties of Mn^{4+}-activated $LiLaMgWO_6$ (LLMW) phosphors for applications in plant cultivation LEDs. The crystal structure and luminescence performance were investigated in detail. Under excitations of 344 nm and 469 nm, the LLMW:$x$$Mn^{4+}$ phosphors showed intense far-red emissions at around 713 nm. The optimal doping concentration of Mn^{4+} ions was 0.7 mol%. The far-red emission band was consistent with the absorption band of phytochrome P_{FR}. Furthermore, the internal quantum efficiency (IQE) and activation energy of the LLMW:0.7% Mn^{4+} phosphors were determined to be as high as 69.1% and 0.39 eV, respectively, suggesting that the LLMW:Mn^{4+} phosphors have excellent optical properties. These results indicate that the LLMW:Mn^{4+} far-red-emitting phosphor-combined NUV chips are promising LED devices as the light source for plant cultivation.

2. Experimental

2.1 Sample preparation

A series of $LiLaMgW_{1-x}O_6$:$x$$Mn^{4+}$ (LLMW:$x$$Mn^{4+}$; x = 0.1%, 0.2%, 0.4%, 0.7%, 1.0%, 1.5%, and 2.0%) phosphors were prepared *via* a high-temperature solid-state reaction method in air atmosphere. Li_2CO_3 (AR), La_2O_3 (99.99%), MgO (AR), $(NH_4)_6H_2W_{12}O_{40}$ (AR), and $MnCO_3$ (AR) in stoichiometric amounts were used as raw materials. All of the reactants were thoroughly ground in an agate mortar and then, the mixtures were transferred to alumina crucibles. Afterwards, the obtained compounds were sintered in a furnace at 1100 °C for 4 h. When the products cooled down naturally to room temperature, they were again ground into powders for further characterizations.

2.2 Characterization

The phase formation and crystal structure of the samples were analyzed by X-ray diffraction (XRD; Bruker D8 Advance) with Cu Kα radiation (λ = 1.54056 Å). Morphology was recorded by using a field-emission scanning electron microscope (FE-SEM; TESCAN MAIA3). Room-temperature photoluminescence (PL) and PL excitation (PLE) spectra were measured by an Edinburgh FS5 spectrometer equipped with a 150 W continuous-wave xenon lamp. The temperature-dependent emission spectra, decay curves, and IQE of the obtained phosphors were also recorded by an Edinburgh FS5 spectrometer equipped with a temperature controller, a pulsed xenon lamp, and an integrating sphere coated with barium sulfate, respectively.

2.3 Fabrication of the LED device

Our red phosphor LLMW:0.7% Mn^{4+} and silicone were mixed thoroughly to obtain a phosphor–silicone mixture. Then, the obtained phosphor–silicone mixture was coated on the surface of the 365 nm LED chip to fabricate a prototype LED device. The fabricated device was driven by 3 V forward voltage and 60 mA current. The photoelectric properties of the fabricated device were measured by using an integrating sphere spectroradiometer system (HAAS2000, Everfine).

3. Results and discussion

The XRD patterns of LLMW:$x$$Mn^{4+}$ (x = 0.1%, 0.7%, 1.5%, and 2.0%) phosphor samples with different Mn^{4+} concentrations are shown in Fig. 1. All diffraction lines were well consistent with those reported for pure $NaLaMgWO_6$ (PDF #88-1761), suggesting that the obtained LLMW:$x$$Mn^{4+}$ samples exhibited single phase and the Mn^{4+} dopant entered the host lattice without significantly influencing the crystal structure.

The Rietveld refinements of LLMW:0.7% Mn^{4+} phosphors, presented in Fig. 2(a), were obtained to further study the crystal structure; the refined crystallographic data are displayed in Table 1. The LLMW compound exhibited a monoclinic crystal structure with the $C2/m$ space group, and the cell parameters were a = 7.8065(6) Å, b = 7.8143(6) Å, and c = 7.8886(6) Å. From the values of the residual factors (R_p = 3.76% and R_{wp} = 5.88%), it can be seen that the refinement results were satisfactory. Furthermore, the peaks in the experimental and calculated spectra were in good agreement. Fig. 2(b) shows the crystal structure of LLMW, in which the W atoms occupied octahedral center sites. It is known that Mn^{4+} can emit red light in the octahedral structure; therefore, Mn^{4+} ions may substitute W^{6+} ions in the LLMW host due to similar ionic radii of W^{6+} (r = 0.62 Å, coordination number (CN) = 6) and Mn^{4+} (r = 0.53 Å, CN = 6) ions.[33,34]

The particle morphology and particle size distribution of the phosphor have direct effects on the fabricated LED device. Fig. 3 represents the SEM micrographs of the LLMW:0.7% Mn^{4+} sample. The observed particle sizes were in the range of 1 to 3 μm, and the particles were uniformly distributed.

Fig. 4(a) shows the PLE and PL spectra of the as-prepared LLMW:0.7% Mn^{4+} phosphors. The PLE spectrum monitored at 713 nm included two main broad bands, which could be well-fitted by four Gaussian curves. In the range of 250–550 nm, the two strong peaks centered at 351 and 476 nm were assigned to spin-allowed $^4A_{2g} \rightarrow {}^4T_{1g}$ and $^4A_{2g} \rightarrow {}^4T_{2g}$ transitions, whereas

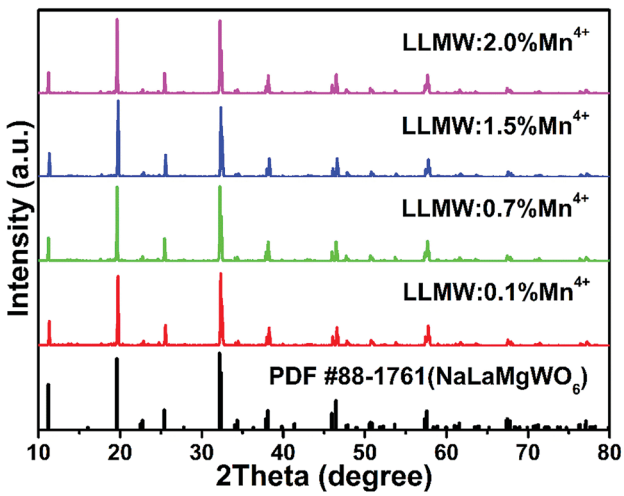

Fig. 1 XRD patterns of LLMW:Mn^{4+} phosphors with different Mn^{4+} concentrations. The standard XRD pattern of $NaLaMgWO_6$ (PDF #88-1761) is shown as a reference.

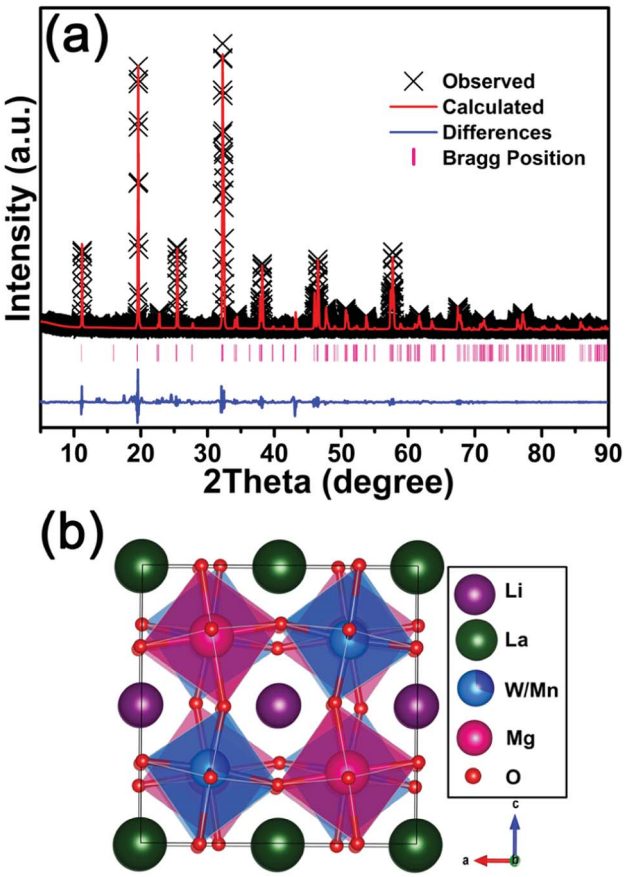

Fig. 2 (a) Rietveld refinements of LLMW:0.7% Mn^{4+} phosphors. (b) Crystal structure of LLMW:0.7% Mn^{4+} phosphors.

the two relatively weak peaks centered at 320 and 403 nm were due to the Mn^{4+}–O^{2-} charge transfer band and the spin-forbidden $^4A_{2g} \rightarrow {}^2T_{2g}$ transition, respectively.[35–37] Upon excitations at 344 and 469 nm, far-red emission bands were observed at 713 nm, corresponding to the spin-forbidden $^2E_g \rightarrow {}^4A_{2g}$ transition,[38–40] which indicated that the phosphors can be excited by NUV (300–380 nm) and blue (420–480 nm) chips.[41] The emission intensity upon excitation at 344 nm was stronger than that upon excitation at 469 nm. Furthermore, a comparison of the absorption spectrum of phytochrome P_{FR} and the emission spectrum of LLMW:0.7% Mn^{4+} phosphors ($\lambda_{ex} = 344$ nm) is displayed in Fig. 4(b). It was clear that there was a broad overlap between the emission band and the absorption band, which implied that the LLMW:Mn^{4+} phosphors could potentially be applied for plant growth.

Table 1 Crystallographic and Rietveld refinement data of LLMW:0.7% Mn^{4+} phosphors

Formula	$LiLaMgWO_6$:0.7% Mn^{4+}
Space group	$C2/m$ – monoclinic
a	7.8065(6) Å
b	7.8143(6) Å
c	7.8886(6) Å
α	90°
β	90.0785(24)°
γ	90°
V	481.22(10) $Å^3$
R_p	3.76%
R_{wp}	5.88%

The PL spectra with variable doping concentration are illustrated in Fig. 4(c). Upon excitation at 344 nm, the profiles of all PL spectra were identical, and the emission intensities varied with the doping concentration as expected. Fig. 4(d) presents the normalized PL intensity of LLMW:$x$$Mn^{4+}$ phosphors as a function of Mn^{4+} dopant concentration. It can be seen that the emission intensity first increased gradually with the increase in Mn^{4+} ion concentration and then decreased when it reached an optimum value. The optimal doping concentration for Mn^{4+} ions was found to be 0.7 mol%, and the phenomenon of the decline in emission intensity was observed due to the concentration quenching effect. Because there was no overlap between the PL and PLE spectra, we inferred that radiation reabsorption did not trigger concentration quenching. According to the theory of Blasse,[42] the nonradiative energy transfer among the nearest Mn^{4+} ions is determined by the critical distance (R_c). Thus, the concentration quenching mechanism can be clarified by using the following equation:[42]

$$R_c = 2\left(\frac{3V}{4\pi x_c N}\right)^{\frac{1}{3}} \quad (1)$$

here, V is the volume of the unit cell, x_c is the critical concentration of the dopant ions, and N refers to the number of available sites for the dopant in the unit cell. For the LLMW:$x$$Mn^{4+}$ phosphors, $V = 481.22$ $Å^3$, $x_c = 0.7\%$, and $N = 4$. Thus, the critical distance (R_c) was calculated to be about 32.02 Å, which was larger than 5 Å, demonstrating that the concentration quenching mechanism in this case was due to electric multipolar interaction rather than exchange interaction. In addition, the type of interaction could be determined by the following equation, which was proposed by Dexter:[43]

$$I/x = K[1 + \beta(x)^{\theta/3}]^{-1} \quad (2)$$

here, I is the emission intensity, x is the activator concentration, K and β are the constants for the same excitation condition, $\theta = 6$, 8, and 10 are consistent with dipole–dipole (d–d), dipole–quadrupole (d–q), and quadrupole–quadrupole (q–q) interactions, respectively.[44] The dependence of $\log(I/x)$ on $\log(x)$ according to eqn (2) is demonstrated in Fig. 4(e), which was fitted well by a line with a slope of $-\theta/3 \approx -1.45$. Hence, the value of θ was calculated to be 4.35, indicating that the concentration quenching mechanism in LLMW:Mn^{4+} phosphors was a d–d interaction.

To further research the nonradiative energy transfer among Mn^{4+} ions, the fluorescence decay lifetimes of LLMW:$x$$Mn^{4+}$ upon excitation at 344 nm were measured, and the decay curves are displayed in Fig. 4(f). All the decay curves could be well-fitted by the following formula:[45]

$$I(t) = A_1 \exp(-t/\tau_1) + A_2 \exp(-t/\tau_2) \quad (3)$$

here, $I(t)$ is the luminescence intensity of the LLMW:$x$$Mn^{4+}$ sample at time t, A_1 and A_2 are constants, τ_1 and τ_2 represent the

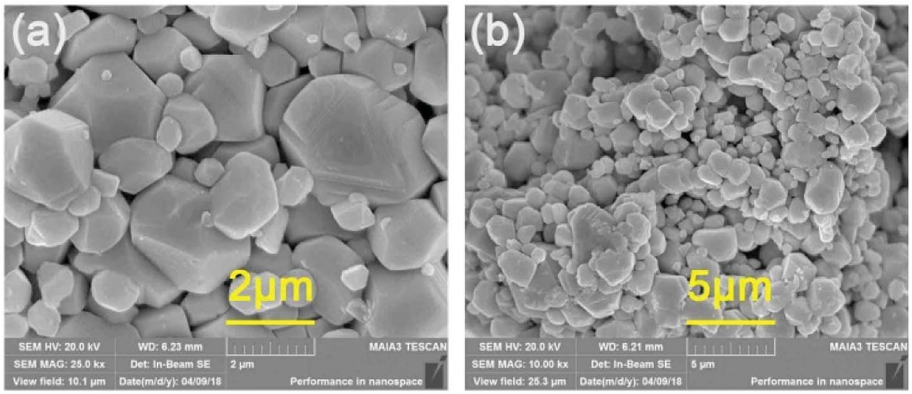

Fig. 3 Representative SEM images of LLMW:0.7% Mn^{4+} phosphors.

lifetimes for the exponential components, and t is the lifetime. The average lifetime, τ_s, can be calculated by using the following equation:[46]

$$\tau_s = (A_1\tau_1^2 + A_2\tau_2^2)/(A_1\tau_1 + A_2\tau_2) \quad (4)$$

All the decay lifetimes were fitted well to a double-exponential decay mode, and the values were in the microsecond range, which was due to the forbidden intra-d-shell transitions of Mn^{4+} ions.[47] In addition, as the doping concentration increased, the lifetimes decreased from 1.791 to 1.579 ms, indicating the existence of nonradiative energy transfer among the Mn^{4+} ions.

When the Mn^{4+} ions are in an octahedral environment, their energy levels depend on the crystal-field environment because of $3d^3$ electron configurations. In this case, the octahedral field of the LLMW host has significant influence on the electron transitions among the different energy levels, which can be illustrated by the Tanabe–Sugano diagram (Fig. 5(a)). Using the mean peak energy (21 008 cm^{-1}) of the $^4A_{2g} \rightarrow {}^4T_{2g}$ transition, the crystal-field strength, D_q, can be obtained by the following equation:[48]

$$D_q = E(^4A_{2g} \rightarrow {}^4T_{2g})/10 \quad (5)$$

The peak energy difference between $^4A_{2g} \rightarrow {}^4T_{2g}$ (21 008 cm^{-1}) and $^4A_{2g} \rightarrow {}^4T_{1g}$ (28 490 cm^{-1}) transitions was found to be 7482 cm^{-1}, and the Racah parameter, B, can be calculated by the formula:[49]

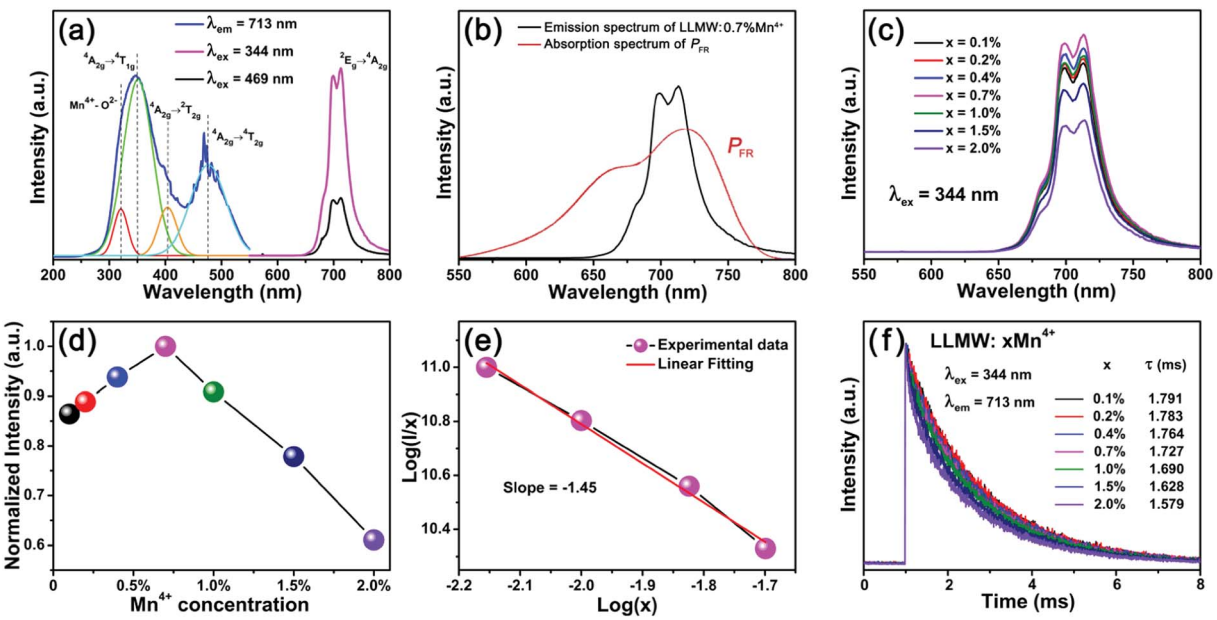

Fig. 4 (a) PLE and PL spectra of LLMW:0.7% Mn^{4+} phosphors. (b) Comparison of the emission spectrum of LLMW:0.7% Mn^{4+} phosphors (λ_{ex} = 344 nm) and the absorption spectrum of phytochrome P_{FR}. (c) PL spectra of LLMW:$x$$Mn^{4+}$ phosphors under 344 nm excitation. (d) Normalized PL intensity of LLMW:$x$$Mn^{4+}$ phosphors as a function of Mn^{4+} concentration. (e) Plot of log(I/x) *vs.* log(x) for the 713 nm emission of Mn^{4+} ions in LLMW:$x$$Mn^{4+}$ phosphors excited at 344 nm. (f) Decay curves of LLMW:$x$$Mn^{4+}$ phosphors excited at 344 nm and monitored at 713 nm.

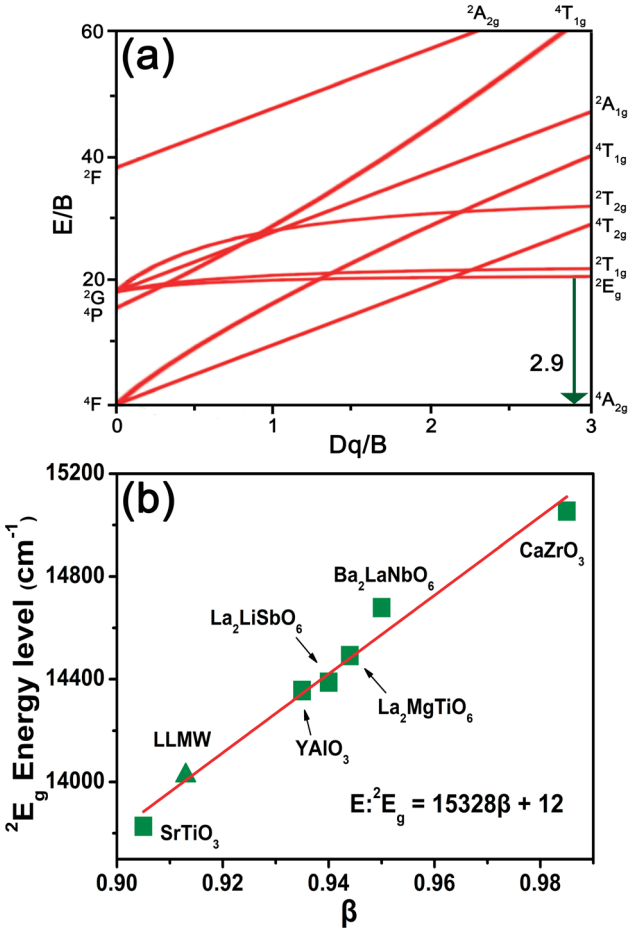

Fig. 5 (a) Tanabe–Sugano diagram of the Mn^{4+} ion. (b) The relationship between the energy of the ^2E_g state and the parameter β.

$$\frac{D_q}{B} = \frac{15(x-8)}{(x^2-10x)} \quad (6)$$

here, x is expressed as follows:

$$x = \frac{E(^4A_{2g} \rightarrow {}^4T_{1g}) - E(^4A_{2g} \rightarrow {}^4T_{2g})}{D_q} \quad (7)$$

The peak energy of the $^2E_g \rightarrow {}^4A_{2g}$ transition was 14 025 cm^{-1}, and the Racah parameter, C, can be determined as follows:

$$E(^2E_g \rightarrow {}^4A_{2g})/B = 3.05C/B + 7.9 - 1.8B/D_q \quad (8)$$

The parameters D_q, B, and C were calculated to be 2101, 724, and 2870 cm^{-1}, respectively. The value of D_q/B, *i.e.*, 2.9 was larger than 2.2; this indicated that in the LLMW host, the crystal field was strong.[50] Moreover, the $^2E_g \rightarrow {}^4A_{2g}$ transition process was almost unaffected by the crystal field; in contrast, the nephelauxetic effect had significant influence on the emission energy of Mn^{4+} ions, which can be investigated with the Racah parameters B and C by the following equation:

$$\beta = \sqrt{\left(\frac{B}{B_0}\right)^2 + \left(\frac{C}{C_0}\right)^2} \quad (9)$$

here, B_0 and C_0 are the Racah parameters for the free state; for Mn^{4+} ions, $B_0 = 1160$ cm^{-1} and $C_0 = 4303$ cm^{-1}. Thus, the value of β in LLMW:Mn^{4+} was calculated to be 0.913, which was similar to those of other perovskites. The value of β and the energy of the $^2E_g \rightarrow {}^4A_{2g}$ emission transition (E:^2E_g) of the Mn^{4+} ions in various perovskites are presented in Table 2. Furthermore, as shown in Fig. 5(b), the energy of the ^2E_g state was linearly related to β (E:$^2E_g = 15328\beta + 12$); this was also observed in the case of LLMW:Mn^{4+} phosphors.

The CIE chromaticity diagram of LLMW:0.7% Mn^{4+} far-red-emitting phosphors upon 344 nm excitation is displayed in Fig. 6(a). After calculations, the CIE chromaticity coordinates of the LLMW:0.7% Mn^{4+} phosphors were found to be (0.7253, 0.2746), and they were located at the deep-red region, satisfying the necessity of phytochrome P_{FR} for far-red light. The inset of Fig. 6(a) shows a digital photograph of the LLMW:0.7% Mn^{4+} phosphors exposed to 365 nm NUV light; it can be seen that the LLMW:0.7% Mn^{4+} phosphors emitted bright light. Furthermore, the CIE chromaticity coordinates of the LLMW:$x$$Mn^{4+}$ samples with different Mn^{4+} doping concentrations are listed in Table 3.

As shown in Fig. 6(b), IQE of the as-prepared LLMW:0.7% Mn^{4+} phosphors was investigated for further study. The value of IQE can be obtained from the following formula:[51]

$$\eta = \frac{\int L_S}{\int E_R - \int E_S} \quad (10)$$

here, L_S is the emission spectrum of the sample, and E_S and E_R are the spectra of the excitation light with sample and with $BaSO_4$ reference, respectively. Under the irradiation of 344 nm, IQE of the LLMW:0.7% Mn^{4+} sample reached up to 69.1%, which was higher than those of Gd_2ZnTiO_6:Mn^{4+} (IQE: 39.7%),[52] La_2MgTiO_6:Mn^{4+} (IQE: 58.7%),[53] and $Ba_2TiGe_2O_8$:Mn^{4+} (IQE: 35.6%).[54] Besides, after excitation at 469 nm, IQE of the as-prepared LLMW:0.7% Mn^{4+} phosphors was 62.6%. The result indicated that LLMW:Mn^{4+} phosphors could be potential far-red emitting phosphors for applications in plant cultivation LEDs.

Generally speaking, thermal stability is a crucial factor in assessing the application of phosphors for LED devices because the LED chips work in a high temperature environment. The temperature-dependent PL spectra of LLMW:0.7% Mn^{4+}

Table 2 Nephelauxetic ratio β and energy of the $^2E_g \rightarrow {}^4A_{2g}$ emission transition (E:^2E_g) of Mn^{4+} ions in various perovskites

Perovskite	β1	E:^2E_g (cm^{-1})	Reference
$CaZrO_3$	0.985	15 054	58
Ba_2LaNbO_6	0.950	14 679	59
La_2MgTiO_6	0.944	14 492	60
La_2LiSbO_6	0.940	14 388	60
$YAlO_3$	0.935	14 356	61
$SrTiO_3$	0.905	13 827	62
$LiLaMgWO_6$	0.913	14 025	This work

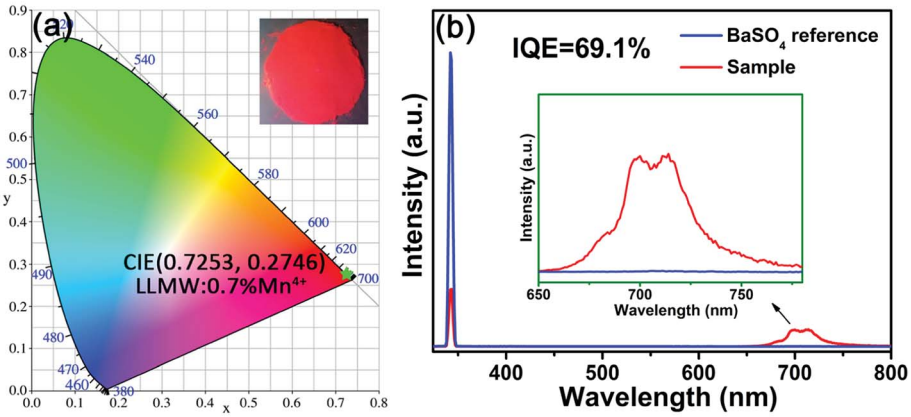

Fig. 6 (a) The CIE chromaticity diagram of LLMW:0.7% Mn^{4+} phosphors at 344 nm excitation. The inset shows the photograph of LLMW:0.7% Mn^{4+} phosphors under a 365 nm UV lamp. (b) The excitation line of $BaSO_4$ and the emission spectrum of LLMW:0.7% Mn^{4+} phosphors collected using an integrating sphere. The inset shows a magnification of the emission spectrum in the 650–780 nm wavelength range.

Table 3 The CIE chromaticity coordinates of LLMW:$x$$Mn^{4+}$ samples with different Mn^{4+} concentrations

Mn^{4+} concentration	CIE chromaticity coordinates (x, y)
0.1%	(0.7230, 0.2769)
0.2%	(0.7239, 0.2760)
0.4%	(0.7251, 0.2749)
0.7%	(0.7253, 0.2746)
1.0%	(0.7249, 0.2751)
1.5%	(0.7240, 0.2760)
2.0%	(0.7222, 0.2778)

phosphors under 344 nm excitation are illustrated in Fig. 7(a). As expected, from 303 K to 503 K, the emission intensity decreased with elevated temperature, which was due to the thermal quenching effect. The inset of Fig. 7(a) shows the normalized intensity of the LLMW:0.7% Mn^{4+} phosphors as a function of temperature; it can be seen that the emission intensity at 423 K was about 49% of its initial value at 303 K. Moreover, to further investigate the thermal quenching effect, the activation energy was calculated by using the following equation:[55]

$$I(t) = \frac{I_0}{1 + c\exp(-E_a/kT)} \quad (11)$$

here, I_0 is the initial emission intensity of the sample at room-temperature, $I(t)$ is the emission intensity at different temperatures, E_a is the activation energy, c is a constant, and k is the Boltzmann constant (8.629×10^{-5} eV). Clearly, E_a can be obtained from the plot of $\ln(I_0/I - 1)$ *vs.* $1/kT$, as shown in Fig. 7(b). Consequently, the value of E_a was determined to be 0.39 eV. The thermal quenching mechanism can be explained by a configurational coordinate diagram, as displayed in Fig. 7(c). The electrons in the ground state, $^4A_{2g}$, jumped to the excited states $^4T_{1g}$ and $^4T_{2g}$ when they absorbed NUV or blue light energy and then, they relaxed to the ^2E_g state through a nonradiative transition. Finally, the excited ions relaxed back to the $^4A_{2g}$ state, giving rise to far-red light centered at 713 nm.[38] At high temperature, some excited electrons absorbed activation energy and transited to the cross-point between the $^4A_{2g}$ state and the $^4T_{2g}$ state;[50] please note that in the end, these excited electrons returned to the ground state $^4A_{2g}$ without fluorescence and thus, this process reduced the emission intensity. Consequently, the higher the activation energy required by the electrons, the better the thermal stability of the phosphors. The value of E_a in this present study was 0.39 eV, which was larger than those of

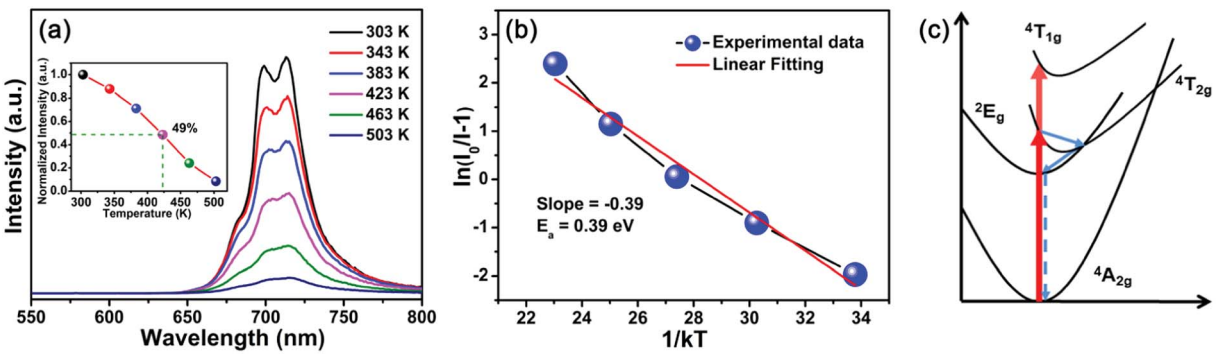

Fig. 7 (a) Temperature-dependent PL spectra of LLMW:0.7% Mn^{4+} phosphors excited at 344 nm. The inset shows the normalized PL intensity of LLMW:0.7% Mn^{4+} phosphors as a function of temperature. (b) Plot of $\ln(I_0/I - 1)$ *vs.* $1/kT$. (c) The configurational coordinate diagram of Mn^{4+}.

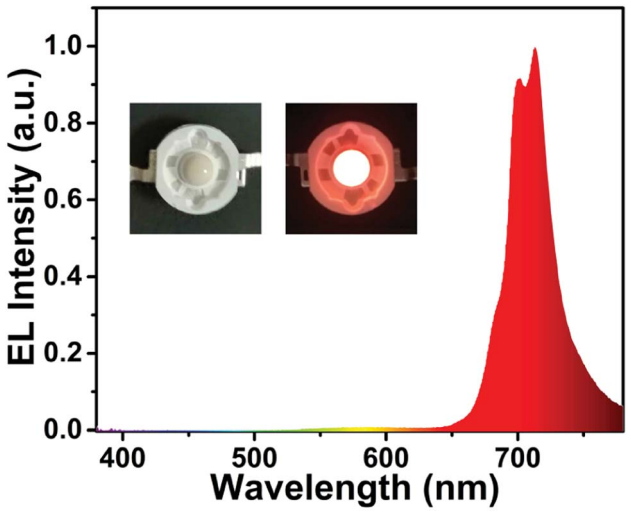

Fig. 8 The EL spectrum of the fabricated red-emitting LED device with a 365 nm NUV chip and LLMW:0.7% Mn^{4+} red phosphors under 60 mA current. The inset shows the fabricated LED device and the corresponding luminescent image.

$Li_2MgTi_3O_8$:Mn^{4+} (E_a: 0.21 eV),[56] Sr_2LaNbO_6:Mn^{4+} (E_a: 0.35 eV)[57] and $Mg_3Ga_2GeO_8$:Mn^{4+} (E_a: 0.22 eV),[47] indicating that the LLMW:0.7% Mn^{4+} phosphors have good thermal stability.

To further verify the potential practical applications of LLMW:$x$$Mn^{4+}$ phosphors, a red-emitting LED device with a 365 nm NUV chip was fabricated. As displayed in Fig. 8, the electroluminescence (EL) spectrum with a far-red emission band centered at 713 nm was consistent with the PL spectra. The inset shows the obtained LED device, which emitted bright red light under 60 mA current and 3 V voltage. Thus, we can conclude that the LLMW:$x$$Mn^{4+}$ phosphors are appropriate for far-red-emitting LEDs in plant cultivation.

4. Conclusion

In summary, a series of Mn^{4+}-activated $LiLaMgWO_6$ far-red-emitting phosphors were synthesized by a traditional solid-state reaction. The as-prepared phosphors could be excited by 344 and 469 nm light; in other words, the phosphors could be excited efficiently by both NUV and blue LED chips. Moreover, the emission peak centered at 713 nm was assigned to the $^2E_g \rightarrow {}^4A_{2g}$ transition, and the optimal doping concentration of Mn^{4+} was 0.7 mol%. The LLMW:0.7% Mn^{4+} phosphors exhibited high IQE (69.1%) and excellent thermal stability (the PL intensity at 423 K was 49% of the initial value at room temperature). The CIE chromaticity coordinates of LLMW:0.7% Mn^{4+} phosphors were (0.7253, 0.2746), which were located in the deep-red range. The emission band showed excellent responsiveness to phytochrome P_{FR}. All these results suggested that LLMW:Mn^{4+} far-red-emitting phosphors have potential applications in plant cultivation LEDs.

Conflicts of interest

There are no conflicts to declare.

Acknowledgements

This work was supported by the National Natural Science Foundation of China (No. 51502190), the Program for the Outstanding Innovative Teams of Higher Learning Institutions of Shanxi, and the Open Fund of the State Key Laboratory of Luminescent Materials and Devices (South China University of Technology, No. 2017-skllmd-01).

References

1 P. Du, X. Huang and J. S. Yu, *Chem. Eng. J.*, 2018, **337**, 91–100.
2 X. Huang, *Nat. Photonics*, 2014, **8**, 748–749.
3 J. Hou, X. Yin, F. Huang and W. Jiang, *Mater. Res. Bull.*, 2012, **47**, 1295–1300.
4 X. Fu, W. Lu, M. Jiao and H. You, *Inorg. Chem.*, 2016, **55**, 6107–6113.
5 X. Huang, S. Wang, B. Li, Q. Sun and H. Guo, *Opt. Lett.*, 2018, **43**, 1307–1310.
6 Z. Ci, Q. Sun, S. Qin, M. Sun, X. Jiang, X. Zhang and Y. Wang, *Phys. Chem. Chem. Phys.*, 2014, **16**, 11597–11602.
7 X. Huang, B. Li, H. Guo and D. Chen, *Dyes Pigm.*, 2017, **143**, 86–94.
8 Z. Ci, M. Que, Y. Shi, G. Zhu and Y. Wang, *Inorg. Chem.*, 2014, **53**, 2195–2199.
9 B. Li, X. Huang, H. Guo and Y. Zeng, *Dyes Pigm.*, 2018, **150**, 67–72.
10 X. Huang, B. Li and H. Guo, *Ceram. Int.*, 2017, **43**, 10566–10571.
11 Z. Ci, Q. Sun, M. Sun, X. Jiang, S. Qin and Y. Wang, *J. Mater. Chem. C*, 2014, **2**, 5850–5856.
12 X. Huang, H. Guo and B. Li, *J. Alloys Compd.*, 2017, **720**, 29–38.
13 X. Huang, *J. Alloys Compd.*, 2017, **690**, 356–359.
14 Z. Ci, R. Guan, L. Jin, L. Han, J. Zhang, J. Ma and Y. Wang, *CrystEngComm*, 2015, **17**, 4982–4986.
15 X. Huang, B. Li and H. Guo, *J. Alloys Compd.*, 2017, **695**, 2773–2780.
16 J. Chen, C. Guo, Z. Yang, T. Li and J. Zhao, *J. Am. Ceram. Soc.*, 2016, **99**, 218–225.
17 L. Li, Y. Pan, Y. Huang, S. Huang and M. Wu, *J. Alloys Compd.*, 2017, **724**, 735–743.
18 J. Long, X. Yuan, C. Ma, M. Du, X. Ma, Z. Wen, R. Ma, Y. Wang and Y. Cao, *RSC Adv.*, 2018, **8**, 1469–1476.
19 P. F. Devlin, J. M. Christie and M. J. Terry, *J. Exp. Bot.*, 2007, **58**, 3071–3077.
20 K. A. Franklin and P. H. Quail, *J. Exp. Bot.*, 2010, **61**, 11–24.
21 T. Nakajima and T. Tsuchiya, *ACS Appl. Mater. Interfaces*, 2015, **7**, 21398–21407.
22 Q. Peng, R. Cao, Y. Ye, S. Guo, Z. Hu, T. Chen and G. Zheng, *J. Alloys Compd.*, 2017, **725**, 139–144.
23 E. Song, Y. Zhou, X. Yang, Z. Liao, W. Zhao, T. Deng, L. Wang, Y. Ma, S. Ye and Q. Zhang, *ACS Photonics*, 2017, **4**, 2556–2565.
24 L. Huang, Y. Zhu, X. Zhang, R. Zou, F. Pan, J. Wang and M. Wu, *Chem. Mater.*, 2016, **28**, 1495–1502.

25 S. Liang, M. Shang, H. Lian, K. Li, Y. Zhang and J. Lin, *J. Mater. Chem. C*, 2016, **4**, 6409–6416.
26 E. Song, J. Wang, J. Shi, T. Deng, S. Ye, M. Peng, J. Wang, L. Wondraczek and Q. Zhang, *ACS Appl. Mater. Interfaces*, 2017, **9**, 8805–8812.
27 L. Li, Y. Pan, Z. Chen, S. Huang and M. Wu, *RSC Adv.*, 2017, **7**, 14868–14875.
28 M. Zhu, Y. Pan, L. Xi, H. Lian and J. Lin, *J. Mater. Chem. C*, 2017, **5**, 10241–10250.
29 L. Xi, Y. Pan, X. Chen, S. Huang and M. Wu, *J. Am. Ceram. Soc.*, 2017, **100**, 2005–2015.
30 J. Zhong, D. Chen, X. Chen, K. Wang, X. Li, Y. Zhu and Z. Ji, *Dalton Trans.*, 2018, **47**, 6528–6537.
31 L. Xi, Y. Pan, M. Zhu, H. Lian and J. Lin, *J. Mater. Chem. C*, 2017, **5**, 9255–9263.
32 M. Zhu, Y. Pan, Y. Huang, H. Lian and J. Lin, *J. Mater. Chem. C*, 2018, **6**, 491–499.
33 X. Huang and H. Guo, *Dyes Pigm.*, 2018, **152**, 36–42.
34 R. Yu, M. Li, N. Xie, T. Wang, N. Xue and H. Guo, *J. Am. Ceram. Soc.*, 2015, **98**, 3849–3855.
35 B. Wang, H. Lin, J. Xu, H. Chen and Y. Wang, *ACS Appl. Mater. Interfaces*, 2014, **6**, 22905–22913.
36 R. Cao, X. Ceng, J. Huang, X. Xia, S. Guo and J. Fu, *Ceram. Int.*, 2016, **42**, 16817–16821.
37 Q. Huang, W. Ye, G. Hu, X. Jiao and X. Liu, *J. Lumin.*, 2018, **194**, 557–564.
38 A. Fu, L. Zhou, S. Wang and Y. Li, *Dyes Pigm.*, 2018, **148**, 9–15.
39 M. Du, *J. Mater. Chem. C*, 2014, **2**, 2475–2481.
40 M. G. Brik, S. J. Camardello and A. M. Srivastava, *ECS J. Solid State Sci. Technol.*, 2014, **4**, R39–R43.
41 W. Lu, W. Z. Lv, Q. Zhao, M. M. Jiao, B. Q. Shao and H. P. You, *Inorg. Chem.*, 2014, **53**, 11985–11990.
42 G. Blasse, *Phys. Lett. A*, 1968, **28**, 444–445.
43 D. L. Dexter, *J. Chem. Phys.*, 1953, **21**, 836–850.
44 H. Guo, X. Huang and Y. Zeng, *J. Alloys Compd.*, 2018, **741**, 300–306.
45 B. Li and X. Huang, *Ceram. Int.*, 2018, **44**, 4915–4923.
46 X. Wu, Y. Jiao, O. Hai, Q. Ren, F. Lin and H. Li, *J. Alloys Compd.*, 2018, **730**, 521–527.
47 X. Ding, G. Zhu, W. Geng, Q. Wang and Y. Wang, *Inorg. Chem.*, 2016, **55**, 154–162.
48 M. J. Reisfeld, N. A. Matwiyoff and L. B. Asprey, *J. Mol. Spectrosc.*, 1971, **39**, 8–20.
49 B. Henderson and G. F. Imbusch, *Optical Spectroscopy of Inorganic Solids*, Clarendon Press, Oxford, UK, 1989.
50 Z. Zhou, J. Zheng, R. Shi, N. Zhang, J. Chen, R. Zhang, H. Suo, E. M. Goldys and C. Guo, *ACS Appl. Mater. Interfaces*, 2017, **9**, 6177–6185.
51 C. Zhang, H. Liang, S. Zhang, C. Liu, D. Hou, L. Zhou, G. Zhang and J. Shi, *J. Phys. Chem. C*, 2012, **116**, 15932–15937.
52 H. Chen, H. Lin, Q. Huang, F. Huang, J. Xu, B. Wang, Z. Lin, J. Zhou and Y. Wang, *J. Mater. Chem. C*, 2016, **4**, 2374–2381.
53 Y. Takeda, H. Kato, M. Kobayashi, H. Kobayashi and M. Kakihana, *Chem. Lett.*, 2015, **44**, 1541–1543.
54 R. Cao, Y. Ye, Q. Peng, G. Zheng, H. Ao, J. Fu, Y. Guo and B. Guo, *Dyes Pigm.*, 2017, **146**, 14–19.
55 S. A. Arrhenius, *Z. Phys. Chem.*, 1889, **4**, 96–116.
56 S. Zhang, Y. Hu, H. Duan, Y. Fu and M. He, *J. Alloys Compd.*, 2016, **693**, 315–325.
57 A. Fu, A. Guan, D. Yu, S. Xia, F. Gao, X. Zhang, L. Zhou, Y. Li and R. Li, *Mater. Res. Bull.*, 2017, **88**, 258–265.
58 M. G. Brik and A. M. Srivastava, *ECS J. Solid State Sci. Technol.*, 2013, **2**, 148–152.
59 A. M. Srivastava and M. G. Brik, *J. Lumin.*, 2012, **132**, 579–584.
60 A. M. Srivastava, M. G. Brik, H. A. Comanzo, W. W. Beers, W. E. Cohen and T. Pocock, *ECS J. Solid State Sci. Technol.*, 2017, **7**, R3158–R3162.
61 M. G. Brik, I. Sildos, M. Berkowski and A. Suchocki, *J. Phys.: Condens. Matter*, 2009, **21**, 025404.
62 Z. Bryknar, V. Trepakov, Z. Potucek and L. Jastrabik, *J. Lumin.*, 2000, **87**, 605–607.